Physica E 140 (2022) 115173

Contents lists available at ScienceDirect

Physica E: Low-dimensional Systems and Nanostructures

journal homepage: www.elsevier.com/locate/physe

Oxygen-injection-dependent nonlinear absorption of MoS_2 colloidal particles fabricated by laser ablation in liquid conditions

Qianbing Cheng [a], Qingyou Liu [b], Ruijin Hong [a,*], Chunxian Tao [a], Qi Wang [a], Hui Lin [a], Zhaoxia Han [a], Dawei Zhang [a]

[a] *Engineering Research Center of Optical Instrument and System, Ministry of Education and Shanghai Key Lab of Modern Optical System, University of Shanghai for Science and Technology, No.516 Jungong Road, Shanghai, 200093, China*

[b] *Key Laboratory of High-temperature and High-pressure Study of the Earth's Interior, Institute of Geochemistry, Chinese Academy of Sciences, Guiyang, 550081, China*

ARTICLE INFO

Keywords:
Oxygen-injection
Plasmonic absorption
Nonlinear absorption (NLA)
Charge transfer

ABSTRACT

A series of colloidal solutions were obtained by pulsed laser ablation (PLA) of MoS_2 ceramic target in water with varying ambient conditions. The results show that the oxygen-injection affects lowering the grain orientation of MoS_2 and improving the monodispersion and plasmonic absorption at the range of 700–1200 nm. The nonlinear absorption (NLA) performance of the oxygen-injection samples is significantly enhanced with the increased oxygen compared with that of the non-oxygen-injection sample. Furthermore, the synergistic effects of electromagnetic enhancement and charge transfer were demonstrated to be the main reason for the improvement of NLA performance.

1. Introduction

In recent years, the research and discovery of nonlinear optical (NLO) materials have received more and more attention. The future generations of optoelectronic devices for information storage, optical switches, and signal processing will mainly rely on the development of materials with exceptional NLO responses [1]. Meanwhile, in the past decade, the effective control of the size, shape and phase of nanoparticles (NPs) has made it more prominent in the NLO applications of biology, medicine, photonics and optoelectronics [2–4]. With the rapid development of nanotechnology, two-dimensional (2D) nanomaterials have received widespread attention due to their unique and fascinating linear and nonlinear characteristics [5–8]. As a special 2D nanomaterials, with excellent optical, electrical, and mechanical properties, graphene has a wide range of applications in materials science, micro-nano processing, biomedicine, etc. [9,10]. The most typical preparation methods is chemical vapor deposition (CVD) technology, which uses a catalytic metal film to prepare large-area and uniform graphene [11,12]. However, when graphene grows on the surface of catalyst mental film, a complicated transfer process is needed [13], which will be damaged during processing, and the process cost is high. Therefore, these adverse factors limit the development of graphene in NLO.

The research of graphene-like materials has greatly changed the research thinking of nanoscience and opened the door to a new two-dimensional nanomaterial [14]. The layered MoS_2 is one of the typical graphene analogs. Its strong in-plane covalent bond and weak out-of-plane van der Waals force form a stable two-dimensional nanostructure [15]. The layered two-dimensional nanomaterials can be synthesized by micromachining and CVD [16]. However, the most suitable method at present is to peel off loose powder from top to bottom by ultrasonic treatment in a specific solvent or water [17,18]. This exfoliation method has been proven in graphene, which can produce a large amount of layered compounds, and then be deposited on the substrate to form a thin film. PLA is a safe and operable green technology that can prepare stable and controllable colloidal nanoparticles [19]. Therefore, PLA has attracted extensive attention in the preparation of nanomaterials such as metal oxides and semiconductors [20]. In 1960, a breakthrough discovery of lasers led to several innovations in determining material properties and developing new nanomaterials [21]. When nanomaterials are exposed to laser, it may induce several NLO effects, such as multiphoton absorption, nonlinear refraction, and so on [22,23]. Moreover, molybdenum trioxide (MoO_3) is an excellent semiconductor material with a wide energy bandgap, which has been widely used in the fields of mode-locked pulsed laser [24], catalysis [25], and so on. MoO_3 nanoparticles (NPs) can be prepared by salt-template

* Corresponding author.
E-mail address: rjhong@usst.edu.cn (R. Hong).

https://doi.org/10.1016/j.physe.2022.115173
Received 11 July 2021; Received in revised form 12 December 2021; Accepted 30 January 2022
Available online 1 February 2022

synthesis [26]. However, these methods are not only complicated but also harmful to the environment. MoO_3 has a wide bandgap and a high degree of recombination of electron-hole pairs generated by light. In this work, PLA technology is used to introduce oxygen defect engineering to improve the performance of MoO_3, reduce the bandgap, improve the life of electron-hole pairs, and significantly enhance the nonlinear absorption [27]. Meanwhile, a large number of electrons are adsorbed around the oxygen vacancies, causing surface plasmon resonance.

In this paper, we prepared MoS_2 colloidal NPs suspension with different concentrations of oxygen vacancies by using Nd:YAG fiber pulsed laser ablation technique. This method presents a good combination of pulsed laser and liquid phase peeling. Moreover, we studied the optical structure and properties of the suspensions with different oxygen vacancies concentrations. The NLO response of the solution was also researched by the ultra-fast laser at 1550 nm.

2. Experiment

We used a molybdenum disulfide (MoS_2) ceramic target (99.99%) with a diameter of 20 mm and a thickness of 5 mm for the experiment. The target's surface was ultrasonic cleaned by acetone to eliminate residues on the of target's surface. The deionized water is heated and boiled to cool to remove the residual oxygen in the water. The target was completely immersed in 6 ml deionized water in a beaker. Then, the solution samples were obtained by laser ablation with a Nd:YAG fiber pulsed laser (wavelength of 1064 nm) at ambient condition. The target was vertically irradiated for 8 min, and the laser parameters are shown in Table 1. It is worth noting that the target should be fully in contact with oxygen in the process of laser irradiation. Therefore, a 100 ml syringe was used to inject oxygen into the solution at a constant rate of 30 ml/min, 60 ml/min, and 90 ml/min in batches. Finally, colloidal particle solutions with different oxygen content were prepared. These solution samples were marked as sample 1 (S1), sample 2 (S2) and sample 3 (S3) (gradient blue solutions), respectively. For comparison, the target was also irradiated without injecting oxygen under the same laser parameters, which was defined as S'. With the varying oxygen contents, the color of colloidal particle solution is also changing. The schematic diagram of the procedure is shown in Fig. 1(a). Furthermore, all the solution samples prepared above have been ultrasonically treated for 2 h, left to stand for 24 h, and then centrifuged at 1000 rpm for 1 h. After centrifugation, the top two-thirds of the dispersion was gently extracted and dropped on the BK9 glass, which then was rotated by a spin coater at a constant speed (400 r/min) for 5 min to prepare the film. Fig. 1(b) shows the mechanism of film preparation by spin coating. The thin film was formed after standing in the air to dry.

The phases of the samples were characterized by X-ray diffraction (XRD, Rigaku MiniFlex 600 system, Japan). The absorption spectra were characterized by a Perkins Elmer double beam spectrophotometer. Raman signals were obtained by the XploRA PLUS Raman spectroscopy with 638 nm laser excitation. Surface analysis of the samples was conducted by the Thermo Scientific Escalab (XPS). The surface morphology was analyzed through scanning electron microscope (SEM) (Merlin compact, Carl Zeiss). The NLO performance of the material was measured by using a mode-locked picosecond laser (Menlosystems, 100 MHz, 2 ps pulse width) at 1550 nm with the same incident intensity and a Gaussian beam focused by a 15 mm focal length lens. Fig. 1(c) shows the Z-scan system.

Table 1
Laser scanning parameter.

Parameter	Unit	Value
Laser	W	8
Beam diameter	Mm	0.01
Pulse width	Ns	200
Frequency	kHz	45
Scanning line spacing	Mm	0.01
Scanning rate	mm/s	100

3. Results and discussion

3.1. Optical structure and properties

The XRD diffraction pattern of the samples with and without oxygen injection is shown in Fig. 2(a). For the sample without oxygen injection, four sharp peaks could be observed at 15.26° (2θ), 40.38° (2θ), 50.66° (2θ), and 61.08° (2θ), corresponding to (002), (103), (105), and (110) of MoS_2 (JCPDS: 39–1492), respectively [7]. Compared with the standard card, the XRD pattern of the sample shifts by 0.8° to the right, which may be due to the residual stress in the material [28]. The strongest diffraction peak is at 15.26° (2θ), indicating the preferred orientation of MoS_2 along (002) crystal plane. These above results show that the laser treatment of the target leads to the formation of MoS_2 NPs with a high crystallization quality. For the samples with oxygen injection, except for the weak diffraction peak of the (002) crystal plane, no other diffraction peaks were detected. This phenomenon indicates that most of the exfoliated MoS_2 NPs were oxidized by oxygen during laser ablation. With the increase of oxygen content, the intensity of diffraction peak at (002) crystal plane gradually decreases, which indicates that the content of MoS_2 NPs reduced. However, due to the poor crystallinity of MoOx, its diffraction peak can not be observed now. Moreover, the broad peak in Fig. 2(a) comes from the BK9 substrate, which could be attributed to that the film thickness is thin with the structure in a discontinuous state, leading to the detection noise of XRD. Furthermore, Table 2 shows the structural characteristics of colloidal NPs with different oxygen contents in deionized water. The laser fluence is fixed at 711 J/cm^2 [3,29]. With the increase of oxygen content, the average size of NPs increases, corresponding to Fig. 5 (d-f).

Fig. 2(b-d) shows the absorption, transmittance and reflectance spectra of all samples, and the inset indicates the enlarged picture of the resonance peak. As shown in Fig. 2(b), There are no obvious absorption peaks for the sample without oxygen injection, and the absorption intensity decreases with the increase of wavelength. This phenomenon verifies the existence of MoS_2 [30]. For the oxygen injected samples, two broad peaks at 742 nm and 976 nm are observed, which are caused by the oscillation of free electrons and transition between bands in the defect MoOx, respectively [31,32]. In addition, due to the introduction of a high concentration of oxygen vacancies, a large number of electrons are adsorbed around the oxygen vacancies, resulting in local surface plasmon resonance [33]. The blue color of the NPs solution is due to the charge transfer transition between Mo ions in various valence states [34]. Moreover, with the increase of oxygen content, the absorption intensity enhances obviously. Fig. 2(c-d) shows transmittance and reflectance of these samples with varying oxygen contents. The results show that the reflectivity of these samples is very low, and most of them are absorption and transmission. The two peaks at 212 nm and 254 nm are corresponding to the peaks of BK9 glass.

3.2. SERS performance

Since the structure change of Mo oxide could not be detected by XRD, Raman spectroscopy was further employed to analyze the initial blue MoOx. Fig. 3 shows the Raman spectra of these samples. The Raman spectra of sample without oxygen injection are shown in the lower part of Fig. 3. The characteristic Raman peaks at 390.7 cm^{-1} and 415.7 cm^{-1} correspond to the $E^1{}_{2g}$ in-plane vibration and A_{1g} out-of-plane vibration of MoS_2 NPs, respectively [35]. The upper part of Fig. 3 reveals the effect of oxygen on the Raman signal of the samples. Three distinct Raman peaks can be observed at 233.2 cm^{-1}, 341.7 cm^{-1}, and 980.1 cm^{-1}, respectively. Precisely, peaks at 233.2 cm^{-1} and 980.1 cm^{-1} correspond to O=Mo=O bending and terminal oxygen (Mo=O) stretching mode, respectively. Due to the introduction of oxygen vacancies, the exfoliated

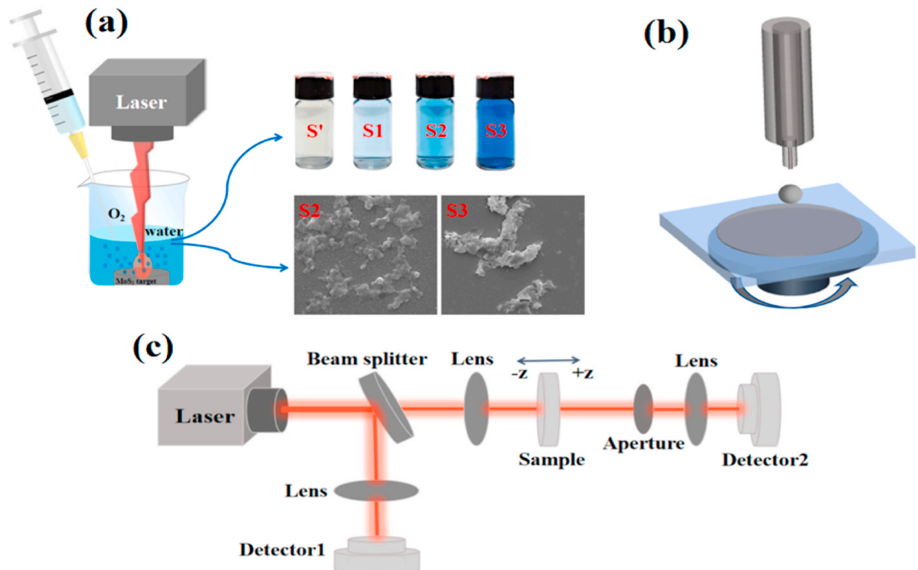

Fig. 1. The schematic for (a) the experiment process, (b) the preparation of thin films by spin coating, and (c) Z-scan system.

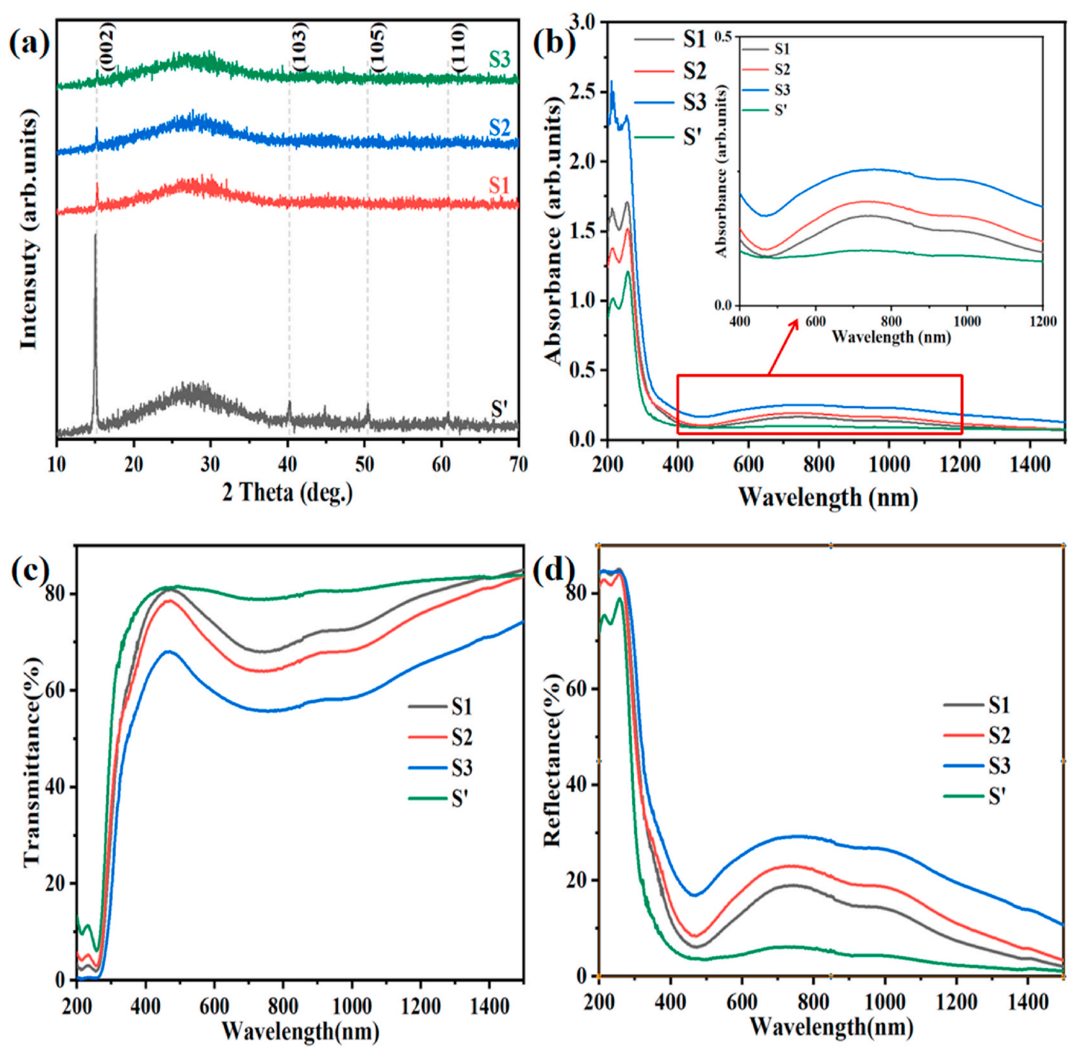

Fig. 2. (a) XRD patterns and (b–d) absorption, transmittance and reflectance spectra of the samples.

Table 2
Structural properties of colloidal nanoparticles with varying oxygen content in deionize water.

Laser fluence (J/cm^2)	2θ	Average Particle size (nm)	Miller indices (*hkl*)	Interplanar distance(d) (Å)	Lattice constants (a and c) (Å)
711 (S′)	15.02	26.49	002	6.1500	a = 3.150 c = 12.300
711 (S2)	15.04	44.35	002	6.1450	a = 3.160 c = 12.300
711 (S3)	15.02	55.84	002	6.1452	a = 3.161 c = 12.295

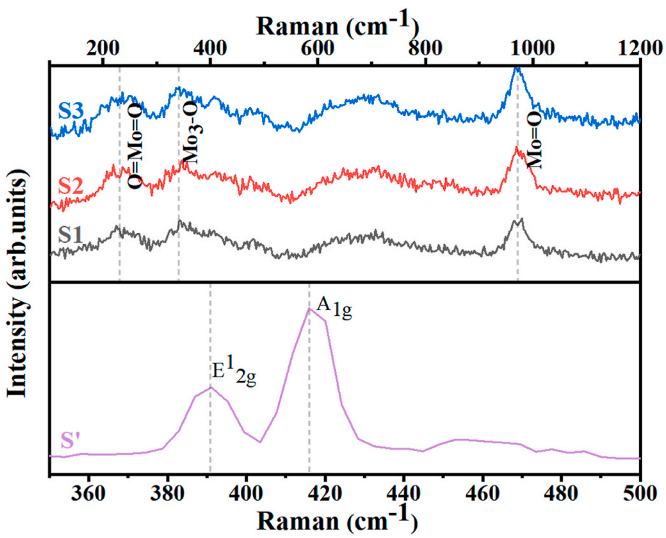

Fig. 3. Raman spectra of the samples with (upper part) and without (lower part) oxygen injection.

MoS_2 interacts with oxygen, and the Raman strength is slightly enhanced, resulting in the separation of photo-generated charges. Meanwhile, the transfer of charge can increase the polarizability of each molecule, which in turn enhances the Raman intensity [36]. The peaks at 341 cm^{-1} represent the triply coordinated oxygen (Mo_3–O) asymmetric stretch mode. This mode illustrates that the edges between three adjacent octahedrons share oxygen atoms [31]. XRD and Raman results show that the crystallinity of the sample without oxygen injection is higher than that of the sample with oxygen injection. The poor crystallinity of the samples may be due to the large crystal defects caused by Mo oxidation in the MoS_2 NPs. Moreover, with the MoS_2 target in contact with oxygen under the thermal effect of laser, a considerable part of the sample is oxidized, resulting in the formation of blue NPs solution and the increased Raman intensity.

3.3. Composition and valence states

The chemical valence and composition of the samples were analyzed by XPS (Fig. 4). To quantify the relative content of each oxidation state, the spectrum was subjected to multi-peak deconvolution. Polluted carbon (284.8 eV) calibration was used to find the correct binding energy of all peaks. Fig. 4(a-c) shows the XPS spectra of Mo 3d without and with oxygenation. Fig. 4(a) reveals the Mo 3d XPS spectra of S' (no oxygen injection). The peaks at 228.2, 229.2, 229.9, 231.5, 232.8 and 233.4 eV represent Mo 3d5/2, Mo^{4+} $3d_{5/2}$, MoS_2, Mo $3d_{3/2}$, Mo^{4+} $3d_{3/2}$, and MoS_2, respectively [37]. In the case of continuous laser ablation, the target was baked into fine particles, which may lead to volatilization of some sulfur due to thermal action, thus forming separate metal molybdenum. Moreover, during the cooling and sampling process, oxygen atoms easily penetrate the MoS_2 lattice structure lacking sulfur to form molybdenum oxide, resulting in the presence of Mo^{4+} [35]. Fig. 4(b) shows the Mo 3d XPS spectrum of oxygen injection at a rate of 60 ml/min (S2). After oxygen injection, some new peaks appeared at 232.23, 233.63, 235.23, and 236.63 eV corresponding to Mo^{5+} $3d_{5/2}$, Mo^{6+} $3d_{5/2}$, Mo^{5+} $3d_{3/2}$ and Mo^{6+} $3d_{3/2}$, respectively [38]. However, Mo^{4+} still exists in the sample, but the content changes, which is due to the high valence Mo ion formed by the reaction of implanted oxygen with MoS_2. With the further increase of injected oxygen (Fig. 4(c)), the tetravalent molybdenum ions could not be observed in the sample, and the contents of Mo^{5+} and Mo^{6+} varied. This is because more oxygen participates in the oxidation reaction Mo^{5+} is converted to Mo^{6+}, which leads to a relative decrease in the Mo^{5+}. Fig. 4(d) shows the O1s spectral peaks of the three samples. The binding energy at 530.68–531.08 eV and 532.03–532.23 eV represent lattice oxygen (lo) and adsorbed oxygen (ao) on the surface of MoOx (such as –OH and H_2O), respectively [33, 39]. The binding energy at 533.18 ± 0.2 eV represents the peak of O1s corresponding to the Mo–O bond of MoOx [31]. Moreover, the increase in oxygen vacancies will lead to a further increase of adsorbed oxygen and asymmetry of the main peak as well [40]. In the three samples we measured, the ratios of lo to ao were 0.656, 0.406 and 0.136, respectively. For S′, there was a large amount of anoxia in the sample due to the lack of oxygen injection. However, for S2 and S3, the ratio is relatively lower. The peak of O1s corresponding to MoOx increases obviously, which may be attributed to more oxygen participating in the oxidation reaction to synthesize MoOx. The existing state and proportion of molecules in the three samples are shown in Table 3. In addition, the results of XPS and XRD are inconsistent, which is due to the poor crystallinity of MoOx coated by liquid spin coating. XPS results show that the difference in oxygen content during laser ablation could change the concentration of oxygen vacancies, thereby affecting the composition of MoOx.

3.4. Surface morphology

The SEM images of the samples with and without oxygen are compared, and the particle size distribution of corresponding samples in Fig. 5. It can be clearly seen that the MoOx in the sample is nonuniform and amorphous state [41], which is consistent with the XRD pattern (Fig. 2(a)). In Fig. 5(a), the MoS_2 NPs were detached from the target by laser ablation and then loaded on the substrate in a flat form without obvious stacking. According to Fig. 5(b) and **(c)**, when oxygen is injected into the solution, the film surface shows the stacking of NPs, that is caused by the increased MoOx with the increase of oxygen content. The insertion diagram in Fig. 5(b) and **(c)** indicates that the grains on the film surface are denser, along with the increase of MoOx content. The increase of MoOx content leads to the increase of absorption intensity, which is consistent with the result shown in Fig. 2(b). Fig. 5(d-f) shows the particle size distributions of these samples measured from SEM images. As the oxygen content increases, the size of the NPs also increases. For S′, S2 and S3, the particle size presents a monodisperse distribution with the average particle sizes of 26.49 nm, 44.35 nm and 77.64 nm, respectively. It is well know that the formation of larger NPs are due to agglomeration tendency of the NPs, which is more prominent in the ablation process [3]. In general, the SEM images are in good agreement with the above experimental results.

3.5. NLO properties

The nonlinear optical properties of the samples were studied using open-hole Z-scan technology. The schematic diagram of the Z-scan device is shown in Fig. 1(c). Fig. 6 shows the normalized transmittance and corresponding nonlinear optical coefficient of the sample in an open-hole Z-scan system with excitation energy of 3.1 × 10^{-3} GW/cm^2 and an excitation wavelength of 1550 nm. In the nonlinear region, the total absorption α can be expressed as $\alpha(I) = \alpha_0 + \beta(I)I$, where α_0, $\beta(I)$, and I represent linear absorption coefficient, nonlinear absorption coefficient

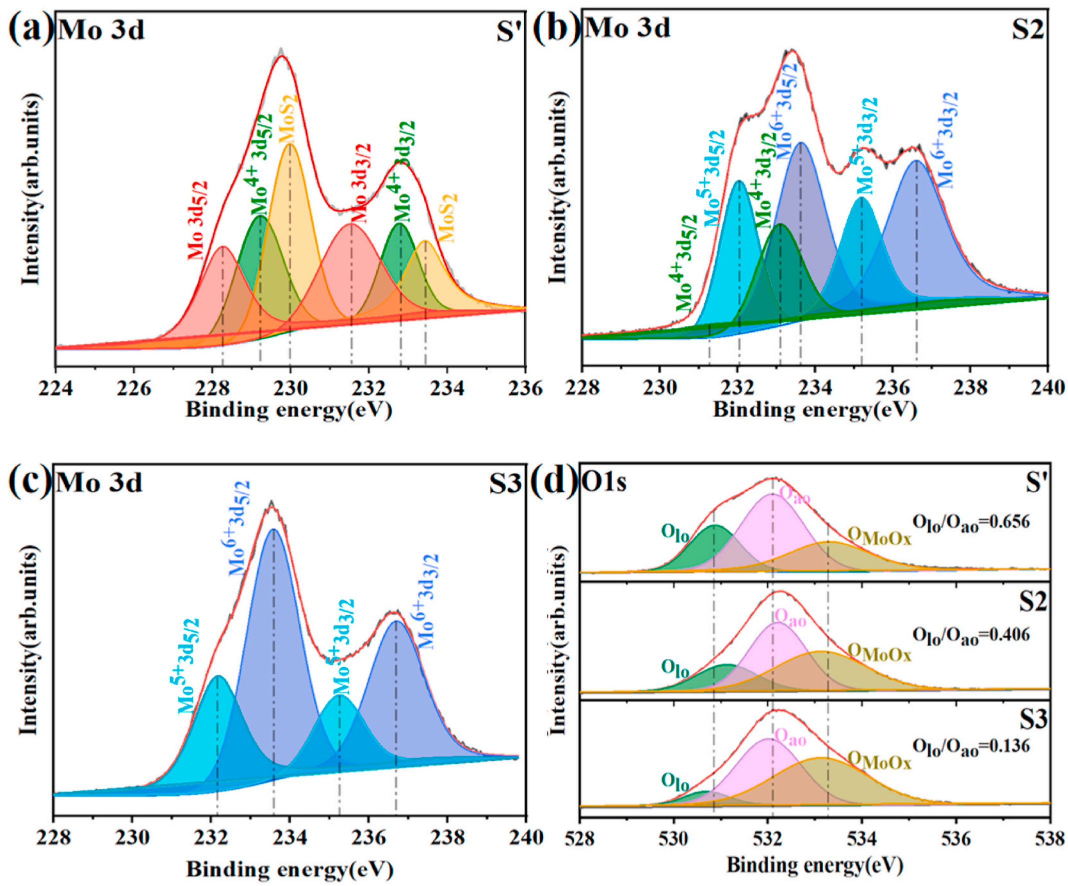

Fig. 4. The XPS spectra of Mo 3d region in (a) S' (without injecting oxygen), (b) S2 (injecting oxygen with 60 ml/min), and S3 (injecting oxygen with 90 ml/min); (d) the XPS spectra of O1s in S′, S2, and S3.

and laser intensity, respectively. In addition, the Z-scan normalized transmittance calculation formula of the sample is as follows:

$$T_{Norm}(z) = 1 - \frac{1}{2\sqrt{2}} \frac{\beta I_0 L_{eff}}{1 + \left(\frac{z}{z_0}\right)^2}$$

Among them, L_{eff} is the effective optical intensity of the samples, the calculation formula can be expressed as $L_{eff} = (1 - e^{-\alpha_0 L})/\alpha_0$, and L is the thickness of the film sample [42]. Moreover, z, z_0, I_0 represent the linear distance from the sample to the focal point, the diffraction length of the beam, and the peak intensity of the sample through the focal point, respectively.

Fig. 6(a) shows the nonlinear absorption (NLA) response of the sample under picosecond laser excitation. Firstly, the Z-scan system was used to test the blank BK9 glass. No NLA phenomenon was found, so the influence of the blank BK9 on the samples could be ruled out. Then, the Z-scan system was used to test the samples without and with oxygen injection. These samples exhibit strong saturation absorption characteristics. In other words, these samples can suppress the transmission of low-intensity light and allow the transmission of high-intensity light. The normalized transmittance values of the samples (S′, S1, S2 and S3) before and after oxygen injection are 1.04, 1.17, 1.25, and 1.45, respectively. Obviously, compared with S′, the normalized transmittance of S1, S2 and S3 is significantly improved. And with the increase of oxygen content, it shows an increasing trend. The NLA coefficient (β) of each sample is shown in Fig. 6(b). These samples show saturated absorption, so β is a negative value. As the laser ablation time increasing (the increased oxygen content), the β of the samples decreases, while the β of the samples without oxygen injection increases. This phenomenon is consistent with the verification result of Z-scan. The difference in laser ablation time causes the sample to introduce different degrees of oxygen vacancy defects. However, the oxygen vacancy is a donor impurity with the minimum generation energy, which plays a vital role in the optical properties. The above experiments prove that the reasonable introduction of oxygen defects can effectively improve the nonlinear performance of the sample.

In order to better understand the NLO properties of MoOx, the energy band diagram in the absence of oxygen and oxygen injection is shown in Fig. 6(c). Eg represents the band gap value of the semiconductor materials, which can be obtained from the results of the absorption spectrum [43]. For the sample without oxygen injection (S′), the band gap is about 1.73 eV. With the introduction of oxygen vacancies (Ovs), the band gap gradually decreases, and the band gap of S2 is 1.43 eV. It is well known that Ov is the donor impurity with the minimum formation energy. Meanwhile, Ovs play key role in changing charge transfer and accelerating electron/hole separation and other optical properties [44,45]. When oxygen is injected into the sample, the prepared films all have different degrees of Ov defects. The introduction of Ovs, the increase in the maximum value of the valence band (VBM), and the expansion of the width of the valence band (VB) lead to the rapid separation of photo-generated charges, thereby enhancing the absorption capacity of the material [24]. In other words, carriers are more easily to be excited from the valence band (VB) to the conduction band (CB), which affects the absorption capacity of the film. In summary, the corresponding enhancement of NLO is largely attributed to the electronic transition between the CB and the defect band.

4. Conclusion

In this paper, colloidal NPs solutions containing different

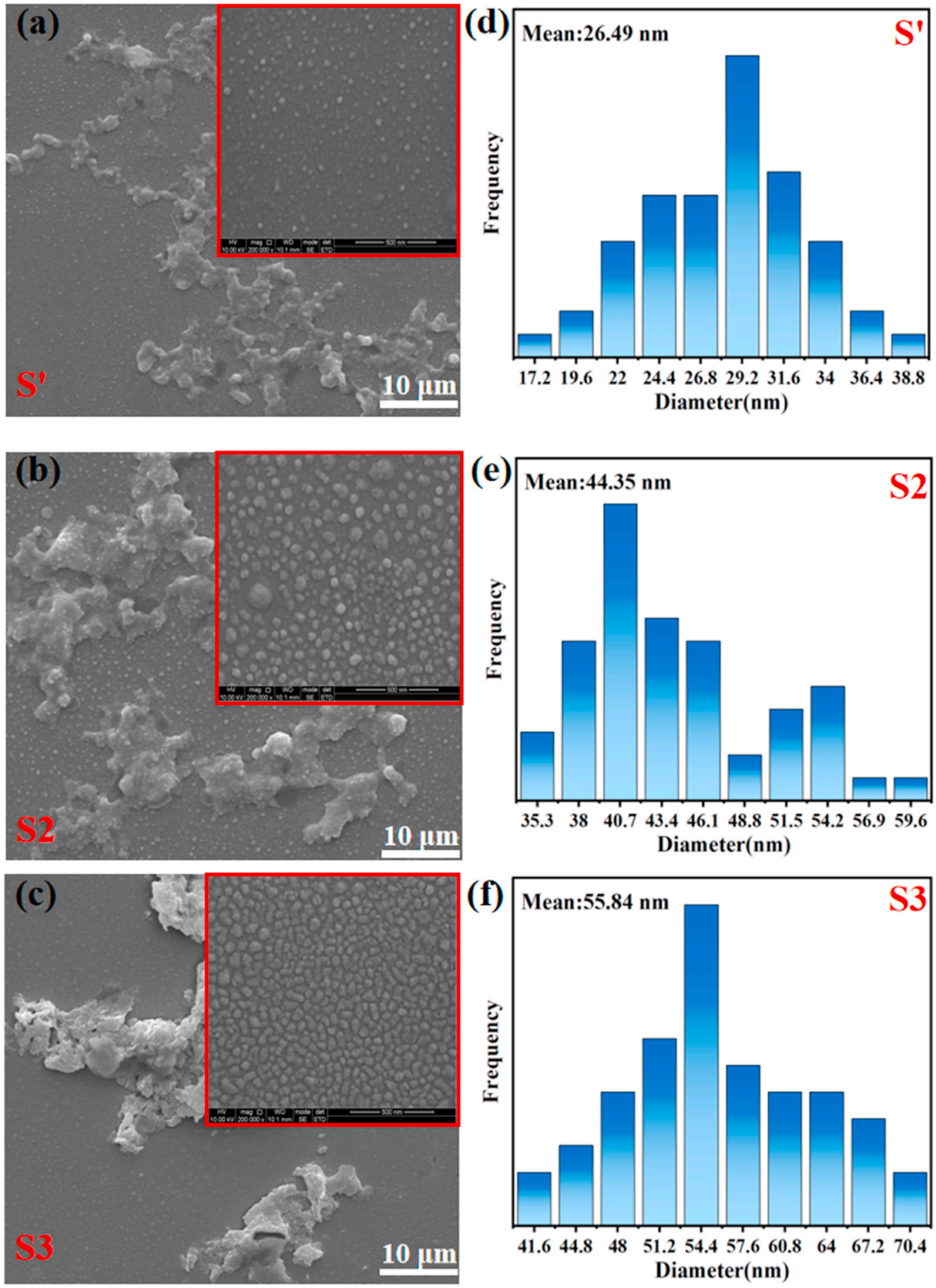

Fig. 5. Scanning electron micrographs (SEM) images of (a) sample ablated without oxygen injection (S′), (b)–(c) samples ablated with oxygen injection at 60 ml/min and 90 ml/min (S2 and S3), respectively. (d–f) Particle size distributions charts of S′, S2 and S3.

Table 3
Relative ratio of molybdenum and oxygen components with different states calculated from the XPS of Mo 3d and O1s Spectra.

	Mo (%)	Mo^{4+} (%)	Mo^{5+} (%)	Mo^{6+} (%)	O_{lo} (%)	O_{ao} (%)	O_{MoOx} (%)
S′	28.03	29.61	0	0	26.98	41.13	31.88
S2	0	20.54	39.30	40.15	18.29	45.07	36.03
S3	0	0	45.25	54.74	6.65	48.88	44.47

concentrations of oxygen vacancies were prepared by laser ablating MoS_2 targets in deionized water. The effects of introducing oxygen vacancies on the surface morphology, composition, and optical properties of the samples were investigated. The results show that the existence of oxygen vacancy leads to the agglomeration of MoOx colloidal NPs. MoS2 and oxygen are transformed into MoOx under the action of pulsed laser, which reduces the grain orientation of MoS2. The enhancement of plasma absorption can be attributed to the charge transfer between conduction band and defect band, resulting in the corresponding enhancement of NLO. The synergistic effect of charge transfer and electromagnetic enhancement largely determines the improvement of

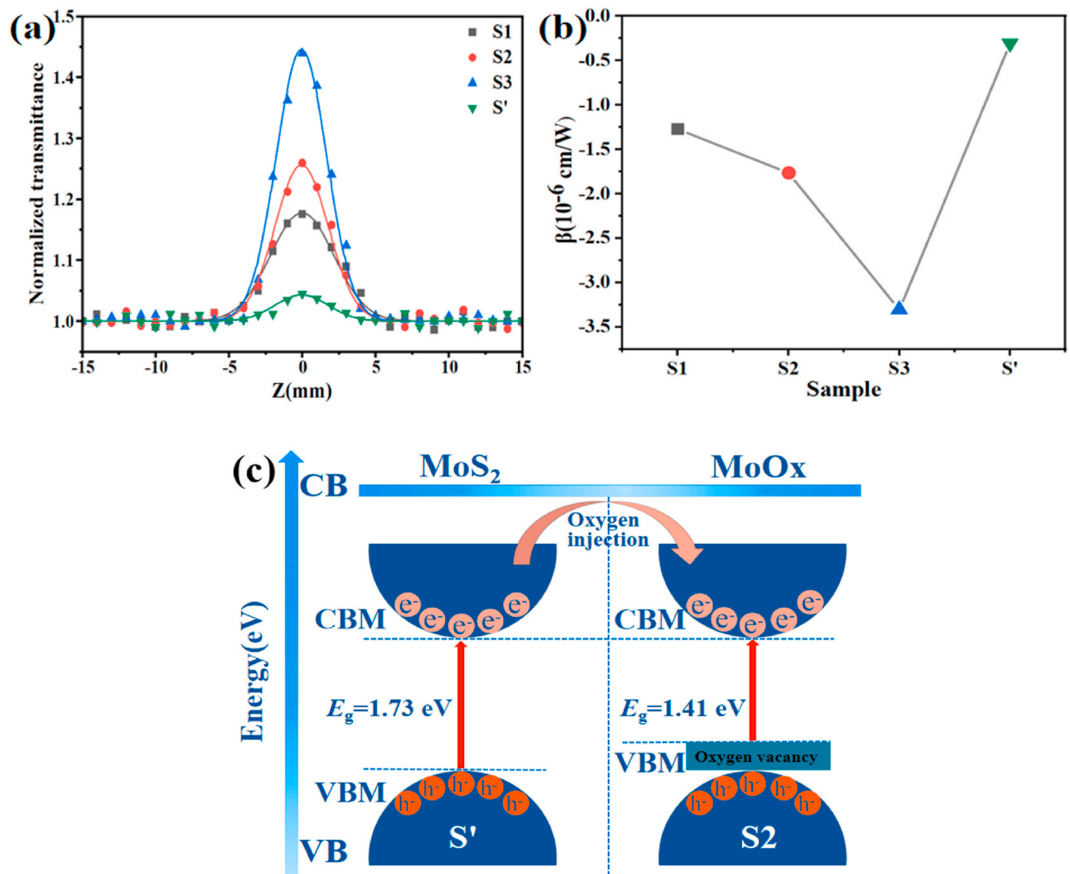

Fig. 6. (a) Open aperture Z-scan curves of the samples; (b) the value of nonlinear absorption (β) of the samples; (c) schematic of the energy band without and with oxygen injection.

NLA performance. This experiment provides a new idea for the engineering research of the NLA characteristics of semiconductor structures and promotes the development and application of plasma-based nonlinear photonic devices.

Declaration of competing interest

The authors declare that they have no known competing financial interests or personal relationships that could have appeared to influence the work reported in this paper: We declare that we have no financial and personal relationships with other people or organizations that can inappropriately influence our work; there is no professional or other personal interest of any nature or kind in any product, service and/or company that could be construed as influencing the position presented in, or the review of, the manuscript entitled.

Acknowledgment

This work was supported by the National Natural Science Foundation of China (61775141, 62075133).

References

[1] P.C. Ray, Size and shape dependent second order nonlinear optical properties of nanomaterials and their application in biological and chemical sensing, Chem. Rev. 110 (2010) 5332–5365.
[2] P. K P, S. E, C. K, S. Varghese, Intense nonlinear optical properties of ZnS quantum dot doped nematic liquid crystal compounds, J. Mol. Liq. 328 (2021).
[3] Y. Al-Douri, S.A. Abdulateef, A.A. Odeh, C.H. Voon, N. Badi, GaNO colloidal nanoparticles synthesis by nanosecond pulsed laser ablation: laser fluence dependent optical absorption and structural properties, Powder Technol. 320 (2017) 457–461.
[4] Y. Al-Douri, Nanosecond pulsed laser ablation to synthesize ternary alloy colloidal nanoparticles, Colloidal Metal Oxide Nanoparticles (2020) 25–38.
[5] M. He, C. Quan, C. He, Y. Huang, L. Zhu, Z. Yao, S. Zhang, J. Bai, X. Xu, Enhanced nonlinear saturable absorption of MoS2/graphene nanocomposite films, J. Phys. Chem. C 121 (2017) 27147–27153.
[6] A. O'Neill, U. Khan, J.N. Coleman, Preparation of high concentration dispersions of exfoliated MoS2 with increased flake size, Chem. Mater. 24 (2012) 2414–2421.
[7] T. Oztas, H.S. Sen, E. Durgun, B. Ortaç, Synthesis of colloidal 2D/3D MoS2 nanostructures by pulsed laser ablation in an organic liquid environment, J. Phys. Chem. C 118 (2014) 30120–30126.
[8] Y. Liu, C. Ma, X. Zhang, H.H. Ngo, W. Guo, M. Zhang, D. Zhang, Role of structural characteristics of MoS2 nanosheets on Pb2+ removal in aqueous solution, Environ. Technol. Innovat. 22 (2021).
[9] J.L. Cheng, N. Vermeulen, J.E. Sipe, Corrigendum: third order optical nonlinearity of graphene (2014New J. Phys.16053014), New J. Phys. 18 (2016).
[10] B. Deng, Z. Xin, R. Xue, S. Zhang, X. Xu, J. Gao, J. Tang, Y. Qi, Y. Wang, Y. Zhao, L. Sun, H. Wang, K. Liu, M.H. Rummeli, L.-T. Weng, Z. Luo, L. Tong, X. Zhang, C. Xie, Z. Liu, H. Peng, Scalable and ultrafast epitaxial growth of single-crystal graphene wafers for electrically tunable liquid-crystal microlens arrays, Sci. Bull. 64 (2019) 659–668.
[11] S. Karamat, S. Sonuşen, Ü. Çelik, Y. Uysallı, A. Oral, Suitable alkaline for graphene peeling grown on metallic catalysts using chemical vapor deposition, Appl. Surf. Sci. 368 (2016) 157–164.
[12] L. Zhou, H. Zhang, H. Bao, G. Liu, Y. Li, W. Cai, Onion-structured spherical MoS2 nanoparticles induced by laser ablation in water and liquid droplets' radial solidification/oriented growth mechanism, J. Phys. Chem. C 121 (2017) 23233–23239.
[13] J. Yang, S. Kumar, M. Kim, H. Hong, I. Akhtar, M.A. Rehman, N. Lee, J.-Y. Park, K. B. Kim, Y. Seo, Studies on directly grown few layer graphene processed using tape-peeling method, Carbon 158 (2020) 749–755.
[14] X. Xia, C. Ma, H. Chen, K. Khan, A.K. Tateen, Q. Xiao, Nonlinear optical properties and ultrafast photonics of 2D BP/Ti3C2 heterostructures, Opt. Mater. 112 (2021).
[15] K. Wang, J. Wang, J. Fan, M. Lotya, A. O'Neill, D. Fox, Y. Feng, X. Zhang, B. Jiang, Q. Zhao, H. Zhang, J.N. Coleman, Ultrafast saturable absorption of two-dimensional MoS2 nanosheets, ACS Nano 7 (2013) 9260–9267.
[16] S. Karmakar, S. Biswas, P. Kumbhakar, Low power continuous-wave nonlinear optical effects in MoS2 nanosheets synthesized by simple bath ultrasonication, Opt. Mater. 73 (2017) 585–594.

[17] A.V. Tyurnina, I. Tzanakis, J. Morton, J. Mi, K. Porfyrakis, B.M. Maciejewska, N. Grobert, D.G. Eskin, Ultrasonic exfoliation of graphene in water: a key parameter study, Carbon 168 (2020) 737–747.
[18] Y. Yu, J. Wang, Preparation of graphene/PMMA composites with assistance of ultrasonic wave under supercritical CO2 conditions, Ultrason. Sonochem. 73 (2021) 105487.
[19] Y. Al-Douri, R.A. Al-Samarai, S.A. Abdulateef, A.A. Odeh, N. Badi, C.H. Voon, Nanosecond pulsed laser ablation to synthesize GaO colloidal nanoparticles: optical and structural properties, Optik 178 (2019) 337–342.
[20] H. Zeng, X.-W. Du, S.C. Singh, S.A. Kulinich, S. Yang, J. He, W. Cai, Nanomaterials via laser ablation/irradiation in liquid: a review, Adv. Funct. Mater. 22 (2012) 1333–1353.
[21] H. Shi, R. Yan, S. Bertolazzi, J. Brivio, B. Gao, A. Kis, D. Jena, H.G. Xing, L. Huang, Exciton dynamics in suspended monolayer and few-layer MoS2 2D crystals, ACS Nano 7 (2013) 1072–1080.
[22] A.K. Kole, S. Gupta, P. Kumbhakar, P.C. Ramamurthy, Nonlinear optical second harmonic generation in ZnS quantum dots and observation on optical properties of ZnS/PMMA nanocomposites, Opt Commun. 313 (2014) 231–237.
[23] B. Gu, Y.-X. Fan, J. Wang, J. Chen, J. Ding, H.-T. Wang, B. Guo, Characterization of saturable absorbers using an open-aperture Gaussian-beamZscan, Phys. Rev. 73 (2006).
[24] H.-Q. Liu, C.-B. Yao, C.-H. Jiang, X. Wang, Preparation, modification and nonlinear optical properties of semiconducting MoS2 and MoS2/ZnO composite film, Opt Laser. Technol. 138 (2021).
[25] P.M. Shafi, R. Dhanabal, A. Chithambararaj, S. Velmathi, A.C. Bose, α-MnO2/h-MoO3 hybrid material for high performance supercapacitor electrode and photocatalyst, ACS Sustain. Chem. Eng. 5 (2017) 4757–4770.
[26] X. Xiao, H. Song, S. Lin, Y. Zhou, X. Zhan, Z. Hu, Q. Zhang, J. Sun, B. Yang, T. Li, L. Jiao, J. Zhou, J. Tang, Y. Gogotsi, Scalable salt-templated synthesis of two-dimensional transition metal oxides, Nat. Commun. 7 (2016) 11296.
[27] S. Sharma, S. Basu, Visible-light-driven efficient photocatalytic abatement of recalcitrant pollutants by centimeter-length MoO3/SiO2 monoliths with long service life, Appl. Mat. Today 23 (2021).
[28] A. D'Elia, G. Cibin, P.E. Robbins, V. Maggi, A. Marcelli, Design and characterization of a mapping device optimized to collect XRD patterns from highly inhomogeneous and low density powder samples, Nucl. Instrum. Methods Phys. Res. Sect. B Beam Interact. Mater. Atoms 411 (2017) 22–28.
[29] J. Liao, Y. Zhan, Q. Liu, R. Hong, C. Tao, Q. Wang, H. Lin, Z. Han, D. Zhang, Tunable surface plasmon resonance of Al-Cu bimetallic nanoparticles thin films induced by pulsed-laser, Appl. Surf. Sci. 540 (2021).
[30] Z. Li, R. Hong, Q. Liu, J. Liao, Q. Cheng, Q. Wang, C. Tao, H. Lin, D. Zhang, b-MoS2 induced the enhancement of nonlinear absorption of Ag thin film, Physica B: Phys. Condens. Matter 591 (2020) 412261.
[31] M. Sajadi, M. Ranjbar, R. Rasuli, Two-step synthesis of Ag-decorated MoO3 nanotubes, and the effect of hydrogen doping, Appl. Surf. Sci. 527 (2020).
[32] Y. Li, J. Wu, G.R. Williams, S. Niu, J. Zhou, Y. Yang, X. Zhang, Z. Fu, D. Li, L.-M. Zhu, Synergistic chemo-photothermal suppression of cancer by melanin decorated MoOx nanosheets, ACS Appl. Bio Mat. 2 (2019) 4356–4366.
[33] R. Hong, Z. Li, Q. Liu, W. Sun, C. Deng, Q. Wang, H. Lin, C. Tao, D. Zhang, Fabrication and photocatalytic property of MoOx nano-particle films from Mo target by laser ablation at ambient conditions, Opt. Mater. 99 (2020).
[34] C. Ni, D. Carolan, J. Hui, C. Rocks, D. Padmanaban, J. Ni, D. Xie, Z. Fang, J. Irvine, P. Maguire, D. Mariotti, Evolution of anodic product from molybdenum metal in absolute ethanol and humidity sensing under ambient conditions, Cryst. Growth Des. 19 (2019) 5249–5257.
[35] T.A. Loh, D.H. Chua, Growth mechanism of pulsed laser fabricated few-layer MoS (2) on metal substrates, ACS Appl. Mater. Interfaces 6 (2014) 15966–15971.
[36] Z. Li, R. Hong, T. Liu, Q. Wang, C. Tao, H. Lin, D. Zhang, The enhancement of nonlinear absorption of Ag thin film on laser induced defective MoOx buffer layer, Chem. Phys. Lett. 754 (2020).
[37] M. Bravo-Sanchez, A. Romero-Galarza, J. Ramírez, A. Gutiérrez-Alejandre, D. A. Solís-Casados, Quantification of the sulfidation extent of Mo in CoMo HDS catalyst through XPS, Appl. Surf. Sci. 493 (2019) 587–592.
[38] U. Rosungnern, P. Kumnorkaew, N. Kayunkid, N. Chanlek, Y. Li, I.M. Tang, N. Thongprong, N. Rujisamphan, T. Supasai, Impact of a spun-cast MoOx layer on the enhanced moisture stability and performance-limiting behaviors of perovskite solar cells, ACS Appl. Energy Mater. 4 (2021) 3169–3181.
[39] X. Shi, X. Chen, X. Chen, S. Zhou, S. Lou, Y. Wang, L. Yuan, PVP assisted hydrothermal synthesis of BiOBr hierarchical nanostructures and high photocatalytic capacity, Chem. Eng. J. 222 (2013) 120–127.
[40] L. Zhang, W. Wang, D. Jiang, E. Gao, S. Sun, Photoreduction of CO2 on BiOCl nanoplates with the assistance of photoinduced oxygen vacancies, Nano Res. 8 (3) (2015) 821–831.
[41] F. He, X. Yin, J. Li, S. Lin, L. Wu, X. Hao, J. Zhang, L. Feng, Characterization of sputtered MoOx thin films with different oxygen content and their application as back contact in CdTe solar cells, Vacuum 176 (2020) 109337.
[42] M. Dinu, F. Quochi, H. Garcia, Third-order nonlinearities in silicon at telecom wavelengths, Appl. Phys. Lett. 82 (2003) 2954–2956.
[43] V. Sharma, V. Maivizhikannan, V.N. Rao, S. Kumar, A. Kumar, A. Kumar, M. V. Shankar, V. Krishnan, Sea urchin shaped ZnO coupled with MoS2 and polyaniline as highly efficient photocatalysts for organic pollutant decomposition and hydrogen evolution, Ceram. Int. 47 (2021) 10301–10313.
[44] P. Zou, Z. Li, P. Jia, G. Luo, C. Wang, Enhanced photocatalytic activity of bismuth oxychloride by in-situ introducing oxygen vacancy, Colloids Surf. A Physicochem. Eng. Asp. 623 (2021).
[45] A. Zhang, R. Gao, L. Hu, X. Zang, R. Yang, S. Wang, S. Yao, Z. Yang, H. Hao, Y.-M. Yan, Rich bulk oxygen Vacancies-Engineered MnO2 with enhanced charge transfer kinetics for supercapacitor, Chem. Eng. J. 417 (2021).